THE ASTROPHYSICAL JOURNAL, 543:868–879, 2000 November 10

MID-INFRARED INTERFEROMETRY ON SPECTRAL LINES. III. AMMONIA AND SILANE AROUND IRC +10216 AND VY CANIS MAJORIS

J. D. MONNIER,[1] W. C. DANCHI,[2] D. S. HALE, P. G. TUTHILL,[3] AND C. H. TOWNES
Space Sciences Laboratory, University of California at Berkeley, Berkeley, CA 94720-7450
Received 2000 January 10; accepted 2000 June 14

ABSTRACT

Using the University of California Berkeley Infrared Spatial Interferometer with a radio frequency (RF) filter bank, the first interferometric observations of mid-infrared molecular absorption features of ammonia (NH_3) and silane (SiH_4) with very high spectral resolution ($\lambda/\Delta\lambda \sim 10^5$) were made. Under the assumptions of spherical symmetry and uniform outflow, these new data permitted the molecular stratification around carbon star IRC +10216 and red supergiant VY CMa to be investigated. For IRC +10216, both ammonia and silane were found to form in the dusty outflow significantly beyond both the dust formation and gas acceleration zones. Specifically, ammonia was found to form before silane in a region of decaying gas turbulence ($\gtrsim 20R_*$), while the silane is produced in a region of relatively smooth gas flow much farther from the star ($\gtrsim 80R_*$). The depletion of gas-phase SiS onto grains soon after dust formation may fuel silane-producing reactions on the grain surfaces. For VY CMa, a combination of interferometric and spectral observations suggest that NH_3 is forming near the termination of the gas acceleration phase in a region of high gas turbulence ($\sim 40R_*$).

Subject headings: circumstellar matter — instrumentation: interferometers — instrumentation: spectrographs — molecular processes — stars: AGB and post-AGB — turbulence

1. INTRODUCTION

Both high- and low-mass stars near the end of their lives are known to emit copious amounts of material, with the high mass-loss rates critically dependent on the formation of silicate or carbonaceous dust grains within a few stellar radii of the red (super-) giant photosphere. Stellar photons both impart momentum to the dust particles through absorption and scattering (which drive a wind) and heat dust close to the star to temperatures of up to 1200–1500 K (e.g., Lafon & Berruyer 1991). Thermal radiation from these hot dust grains peaks in the near-infrared (1–5 μm), while more distant and cooler (500 K) grains emit mostly in the mid-infrared (5–20 μm).

Although the physical sizes of these evolved stars are impressive ($R_* \gtrsim 1$ AU), their galactic paucity means that even the closest examples lie at distances greater than 50 pc. Thus, the characteristic size scale for dusty circumstellar emission at a few stellar radii is generally a small fraction of an arcsecond, too small to be resolved using standard observing techniques from ground-based telescopes limited by telescope diffraction (in the mid-IR) and/or atmospheric turbulence (for shorter wavelengths). However, long-baseline interferometry in the infrared can directly detect and measure the morphologies of these envelopes.

The high densities of heavy elements and the mild temperatures around evolved stars encourage the formation of myriad diatomic and polyatomic molecules in addition to dust grains. For instance, over 50 molecular species have been found around the prototypical carbon star IRC +10216 (see review by Glassgold 1998). Attempts to understand the density, temperature, and velocity distributions, as well as the formation mechanisms of these molecules, have contributed to the development of the field of astrochemistry.

Using estimates of the temperature, atomic abundances, and gas density in and above the photosphere, predictions of molecular abundances can be made through detailed calculations of a network of chemical reactions. By assuming local thermodynamic equilibrium (LTE), various molecules are said to "freeze out" in the stellar wind. The decreasing temperatures and densities cause reaction rates to fall quickly, locking the atoms in certain energetically favorable molecules. Frozen equilibria models have proven useful in explaining the abundances of many molecules observed around asymptotic giant branch (AGB) stars (e.g., Lafont, Lucas, & Omont 1982); however, additional chemical processes are needed to explain some detected species. For instance, penetration of interstellar UV radiation catalyzes photochemical reactions in the outer envelopes of AGB stars (e.g., Cherchneff & Glassgold 1993), while other molecules may be produced under nonequilibrium conditions associated with shocks (Willacy & Cherchneff 1998). Particularly relevant here is the fact that negligible amounts of silane and ammonia are predicted by most freeze-out models, yet they have been detected with some abundance in circumstellar envelopes (e.g., Keady & Ridgway 1993, hereafter KR93); their formation is hypothesized to be catalyzed on the surfaces of dust grains in the flow. In addition, recent discoveries of brown dwarfs and extrasolar planets have catalyzed interest in the chemistry of cool stellar atmospheres (e.g., Burrows & Sharp 1999), leading to new insights into molecular formation mechanisms in these environments. Since it is often difficult or impossible to experimentally reproduce the physical conditions of circumstellar and interstellar space, molecular observations are critical to test and guide relevant theories.

This paper is the third in a series on the spatial distribu-

[1] Current address: Smithsonian Astrophysical Observatory, MS 42, 60 Garden Street, Cambridge, MA, 02138.
[2] Current address: NASA Goddard Space Flight Center, Infrared Astrophysics, Code 685, Greenbelt, MD 20771.
[3] Current address: Chatterton Astronomy Department, School of Physics, University of Sydney, NSW 2006, Australia.

tions of dust and molecules in the inner envelopes of nearby red giants and supergiants. Paper I (Monnier et al. 2000b) discussed the hardware implementation of this experiment, while Paper II (Monnier et al. 2000a) discussed recent visibility data at 11.15 μm and presented the appropriate dust shell models for IRC +10216 and VY CMa. This paper (Paper III) makes use of these results, as well as the first mid-IR visibility data ever reported on spectral lines, providing critical new information on the molecular stratification around these stars.

The methods used in this work are technologically challenging and represent significant advances in infrared interferometry. By combining the high spatial resolution of long-baseline interferometry with the high spectral resolution of heterodyne spectroscopy (Paper I), this work has, for the first time, probed the brightness distribution on and off spectral absorption features as narrow as ~ 1 km s^{-1} ($\lambda/\Delta\lambda \sim 10^5$). This allows the absorbing regions of polyatomic molecules to be directly measured, setting strong limits on the formation radii. Such measurements are important for determining the formation mechanism, since there is at present no good theory to explain the observed high abundance of certain molecular species (e.g., NH_3 and SiH_4).

2. MODELING

The observing methodology for extracting visibility data on and off spectral lines with the Infrared Spatial Interferometer (ISI) has been discussed in detail in Paper I and Monnier (1999). New dust shell models of IRC +10216 and VY CMa have been developed in Paper II. However, interpreting spectral line observations requires modeling of the distribution of circumstellar molecules as well as dust.

As for observations of continuum radiation with the ISI, it is rarely possible to directly reconstruct an image of the astrophysical source, due to the sparse sampling of the Fourier plane afforded by a two-element interferometer. This limitation necessitates the use of radiative transfer models for interpreting the line data. This section discusses the assumptions used in creating models of the molecular envelopes around AGB stars, the numerical code, and the scientific goals of subsequent analyses.

2.1. *Simple Models*

Paper II adopted assumptions of a spherically symmetric and uniform outflow of dust embedded in the stellar winds, approximations that have been extended to include the distribution of molecular material. As with the models of the dust shells, the molecular envelope was characterized by the inner formation radius and overall abundance factor, free parameters in fitting models to the molecular line data.

Observations have shown that the line shapes of SiH_4 and NH_3 around AGB stars typically show emission in the red wing and absorption in the blue (e.g., Goldhaber 1988, hereafter G88). This kind of profile is expected for molecular emission and absorption in an expanding envelope (e.g., Shu 1991). Figure 1 shows a theoretical line profile similar to those actually observed. The bulk of the absorption is blueshifted with respect to the star at the speed of the outflow. This is because the entire column of molecular gas along the line of sight connecting the observer and the star is at the same relative velocity ($-v_{\rm outflow}$), assuming uniform outflow; hence, there is a large optical depth, $\tau_{\rm line}$, at this frequency, and self-absorption is observed. On the other hand, lines of sight that penetrate the molecular gas

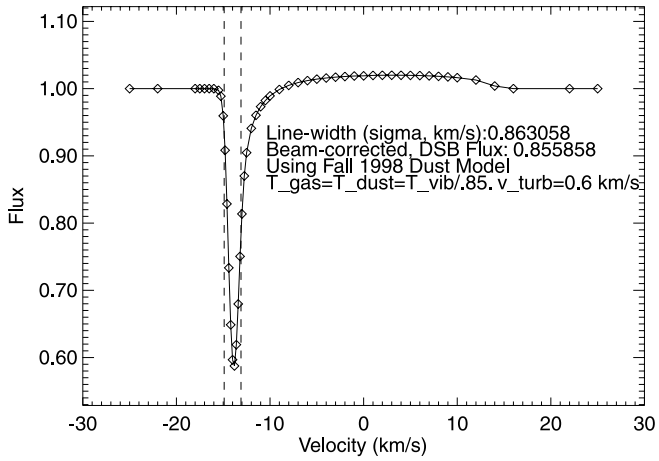

FIG. 1.—Example of a theoretical spectral line shape using radiative transfer calculations from the Keady (1982) code.

envelope at impact parameters off the observer-star axis encounter parcels of gas at a variety of relative Doppler shifts. The optical depth at any particular frequency is hence generally low, allowing emission from deeper layers of hot dust to escape and to be observed without significant molecular absorption. The low-level emission observed at both blue- and redshifted velocities arises from the relaxation of IR-pumped and collisionally excited transitions into higher energy vibrational states. Note that absorption in the line core occurs primarily because of the large optical depth at that frequency, combined with the fact that the temperature decreases with increasing distance from the star. Hence, absorption under these conditions would occur even when the molecules are in local thermodynamic equilibrium (LTE) with the dust and radiation.

For the AGB stars studied here, the source of most of the mid-IR flux is thermal emission from the dust envelope (Danchi et al. 1994), not from the star itself. Since the blueshifted absorption features indicate that most of the absorption is occurring along the direction toward the center of dust envelope, an interesting measurement that can be made with an interferometer is the size of the absorption region. This measurement yields direct information on the approximate location of the $\tau_{\rm line} \sim 1$ surface, which can be used to determine the abundance and inner radius of molecular formation. However, this method is insensitive to molecules that may exist right at the inner radius of the dust, if they are in LTE. This is because there is no significant background source of radiation to absorb. These complications require the use of a sophisticated spectral line code to quantify the sensitivity of this method to molecules forming near the inner radius of the dust shell. Such a code has been used, and is described in the next section.

Previous spectral line work (Betz, McLaren, & Spears 1979, hereafter B79; McLaren & Betz 1980; Goldhaber & Betz 1984; G88; KR93) has shown that ammonia and silane exist around AGB stars at up to 10^4 times the abundances predicted by equilibrium calculations of expanding outflows (for more recent work under somewhat different physical conditions, see Burrows & Sharp 1999). It has been suggested that dust catalyzes the formation of these molecules through chemical reactions on grain surfaces. If this is the case, one might expect the inner radius of molecular formation to coincide with the dust formation radius. However, atoms and molecules generally have low sticking

efficiencies at high temperatures, elastically scattering off the grain surfaces (e.g., Leitch-Devlin & Williams 1985). This fact, and the lack of known chemical pathways for the formation of molecules such as ammonia and silane, make direct measurements of molecular formation radii important, and this is one of the primary goals of the filter-bank project of the ISI.

2.2. *Radiative Transfer Calculations*

Radiative transfer in spectral lines often is accomplished by applying the Sobolev approximation (e.g., G88; Shu 1991), which assumes that large-scale velocity gradients essentially radiatively decouple parcels of molecular gas. To accurately calculate the radiative transfer in a spectral line, the Sobolev approximation requires the natural line width, in this case determined by microturbulence (for cold gas) or thermal motions (for hot gas), to be much smaller than the expansion velocity. While this condition is reasonably satisfied for the narrowest lines ($v_{\rm outflow} \sim 15\,\Delta v_{\rm line\ width}$), it is only weakly so for the broadest ones ($v_{\rm outflow} \sim 4\,\Delta v_{\rm line\ width}$).

In order to avoid this uncertainty, all radiative transfer calculations in spectral lines were performed using a code developed by J. J. Keady (Keady 1982), based on the method of Mihalas, Kunasz, & Hummer (1975). It accurately calculates line profiles as well as frequency-dependent emission profiles, from which visibility curves can be computed on and off spectral features. This code was developed to treat the case of molecules embedded in an expanding flow, even when the absorbing molecules are comingled with continuum-emitting sources. This is likely the case for AGB stars, where thermal emission by dust is believed to be "filling-in" the absorption features. The program, written in Fortran, formally solves the observer's frame transport equation, which is necessary to correctly account for the propagation of line radiation through an expanding flow, thus avoiding the questionable Sobolev approximation. Keady has allowed his code to be used for the analyses that follow, and has assisted in porting the Fortran code to run under Solaris. This code has been extensively tested, having been used for over 15 yr (Keady 1982; Keady, Hall, & Ridgway 1988; KR93; Winters et al. 1998). While the code was already able to be used with spherical top molecules (e.g., SiH_4), the appropriate partition function and statistical weights had to be programmed for NH_3 (a symmetric rotor). A nice summary of the mid-IR molecular properties of both SiH_4 and NH_3 can be found in chapter 5 of G88. Readers interested in the numerical details of the radiative transfer calculation should consult Keady (1982) and Mihalas et al. (1975) for further details.

2.3. *Assumptions*

2.3.1. *Dust*

The source function used for radiative transfer in Keady's code assumes a single dust grain size and temperature at a given radius from the star. The code (Wolfire & Cassinelli 1986) that was used for fitting the ISI continuum visibility data in Paper II utilized the full MRN (Mathis, Rumpl, & Nordsieck 1977) distribution of grain sizes, and hence some modification must be made to adopt our previous models for use by Keady's algorithm. The average cross section of the MRN distribution was used as input to the Keady code, along with the size-averaged dust temperature. This necessary simplification resulted in a slight misfit to the ISI continuum visibility data, which was compensated for by empirically adjusting the overall value of the single grain size dust opacity ($\lesssim$30% change).

2.3.2. *Temperature(s) of the Gas*

In addition to spherical symmetry and uniform outflow, other assumptions are also generally made for line calculations. Most important is the assumption that the occupation of various rovibrational states of the polyatomic molecules can be approximated by a Boltzmann distribution using separate vibrational and rotational temperatures, $T_{\rm vib}$ and $T_{\rm rot}$. Ideally, the populations of the various states should be calculated using a multilevel model molecule. However, the collisional excitation constants are poorly known for SiH_4 and NH_3, and the large number of (far-IR) rotational transitions make for a difficult and uncertain result.

G88 (p. 103) considered this question in some detail for IRC +10216, and we summarize his conclusions here. For sufficiently high molecular densities, both mid- and far-IR (i.e., rovibrational and pure rotational) transitions will be optically thick, trapping line radiation. In this case, collisional excitation and de-excitation will have a strong influence on the level populations, equilibrating the vibrational and rotational temperatures with the gas (kinetic) temperature. However, the molecules under consideration here are not found at sufficiently high densities for this to apply.

At the somewhat lower densities encountered for ammonia and silane, the mid-IR (rovibrational) transitions become optically thin. In terms of excitation mechanism, this allows IR pumping of the vibration-rotation transitions to dominate (over collisions) within about $70R_*$, while rotational relaxation in the pure rotational transitions (far-IR) dominate in the outer envelope (where these transitions become optically thin). Collisional excitation and de-excitation never play a dominant role. Hence, $T_{\rm vib}$ and $T_{\rm rot}$ should be close to the radiation/dust temperature, $T_{\rm dust}$, suggesting that $T_{\rm vib} = T_{\rm rot} = T_{\rm dust}$ is a good starting point. The radial dependence of the rotational and vibrational temperatures usually need slight adjustment during the modeling process to reproduce the relative depths of high- and low-excitation lines.

One interesting exception applies to the $J = K$ states of NH_3. The rotational dipole moment along the symmetry axis (z-axis) of NH_3 is equal to zero; hence, the $\Delta K = 0$ selection rule must apply for all radiative (dipole) transitions (see Townes & Schawlow 1975). Therefore, a molecule rotating in the $J = K$ state cannot radiatively de-excite to a lower energy (lower J) state. Hence, the equilibrium population of $J = K$ states is *not* determined by the radiation temperature, but by collisions with the ambient gas (mostly H_2); the rotational temperature of these states should be in equilibrium with the gas (kinetic) temperature. However, a strong (parallel-type) vibrational band at 6.1 μm does allow $\Delta K = \pm 1$ transitions, thereby allowing K-ladders to come into equilibrium if sufficiently excited by the radiation field. Sufficient IR pumping in this band is likely to dominate over collisional processes out to a few hundred R_*, although a detailed calculation is lacking (see G88).

2.3.3. *Molecular Constants*

The polyatomic molecules of SiH_4 and NH_3 have been modeled using physical constants (see Table 1), including the moments of inertia and vibrational energy levels,

TABLE 1

MOLECULAR CONSTANTS ASSUMED IN THE MODEL CALCULATIONS

Parameter	Value	Source
	SiH_4	
B	2.8591 cm^{-1}	1
ν_4	913.473 cm^{-1}	1
μ_4	0.247 D	2
	NH_3	
B	9.9466 cm^{-1}	3
$C - B$.....	−3.7199 cm^{-1}	3
ν_2	932.434 cm^{-1}	3
μ_2	0.24 D	4

NOTE.—Most of these parameters were originally collected in Goldhaber (Table V.1 in G88). The rotational constants (B and C) are given for the vibrational ground state, along with the appropriate vibrational dipole moment (μ_n) and origin frequency (ν_n).

REFERENCES.—(1) Gray, Robiette, & Johns 1977; (2) KR93; (3) Urban et al. 1983; (4) Nakanaga, Kondo, & Saeki 1985.

adopted from KR93 and G88. Readers interested in learning more about molecular spectroscopy should consult these sources; a rigorous and complete treatment of the subject can be found in *Microwave Spectroscopy* by Townes & Schawlow (1975).

2.4. *Analysis Method*

For each star and target molecule, the analysis strategy for ISI spectral line data was straightforward and had three major steps.

1. The dust shell was modeled in order to have a reasonable approximation of the continuum source. This has been done in Paper II, where coeval continuum visibility data were used to create appropriate dust shell models of the astrophysical sources under study.

2. Molecules were assumed to form at a given radius from the star and to flow out uniformly. Theoretical spectral line profiles were then calculated to fit both ISI measurements and also previous observations of spectral line depths and ratios. Lines of various excitation energies were used (when available) in order to probe the abundance, temperature, and turbulent structure of the gas. This level of analysis relied heavily on the careful modeling preexisting in the astrophysics literature.

3. Theoretical visibilities on and off the spectral line were calculated and compared to the observed visibility ratios. The radius of molecular formation set in step 2 was varied until all available data were satisfactorily fitted.

This method allows one to distinguish between gas models with high molecular abundance far from the star and those with lower molecular abundance close to the star in two different ways. While the line depth of a given transition can always be fitted by varying the abundance and mean gas temperature, the relative line depths of transitions with different excitation energies cannot. This probe of the average excitation temperature, when coupled with estimates of the radial temperature profile and assumption of uniform outflow, can be used to infer the location of molecular formation (e.g., KR93). In this work, we also apply a second, more direct, approach by using an interferometer. With suitable spectral and spatial resolution, one can directly detect the absorption pattern when the molecules are sufficient close to the star. This is the main thrust of this paper, in which we show that molecules within $40R_*$ would significantly modify the emission pattern in the line core, providing a method independent of the line ratio argument for detecting the presence of molecules close to the star.

2.5. *Comparing Model Quantities to Observations*

After fully specifying the dust and gas characteristics, the Keady code returns a spectral line profile and monochromatic radial emission profiles. This section discusses some of the details regarding comparison of the modeling results with ISI filter-bank data.

2.5.1. *Spectral Line Profiles*

Because of the heterodyne detection scheme, mid-IR radiation arriving outside the primary beam of the interferometer was not seen. This had a small effect on the depth of the spectral line, since only a fraction of the molecular absorption occurs in the outer envelope. The effect was compensated for by multiplying the angular distribution resulting from monochromatic radial emission calculations by the effective primary beam of FWHM 3″ (see Paper II for more discussion) and then adjusting the flux level accordingly. All spectral profiles shown in the next sections have had this correction applied.

Next, the finite bandwidth of the filter-bank observations and the double-sideband (DSB) nature of the detection were accounted for. The bandpass center frequency and width were used to determine the average depth of the calculated spectral line for a corresponding single-sideband (SSB) observation. The dilution of the line depth due to the combination of the "uninteresting" additional continuum sideband encountered in practical observation was accounted for by dividing the SSB line depth by 2. This resulting DSB (diluted) line depth was then compared to observations with the filter bank.

Figure 1 shows one of the output figures from the modeling analysis suite. The bandwidth of the observation is marked off by vertical dashed lines, and line diagnostics have been calculated. The line width and average DSB line depth were also calculated for comparison with spectral line observations. Other quantities were also determined, such as the equivalent width, which were useful when comparing with lower spectral resolution data.

2.5.2. *Visibility Ratios*

The basic observable of the filter-bank experiment is the visibility ratio on the spectral line compared to the dust continuum. Monochromatic radial emission profiles were calculated at 10 specific frequencies across the spectral line, sampling the stellar continuum as well as the entire absorption region. The double-sideband, radial-emission profile for the finite bandwidth selected by the filter bank was determined by a flux-weighted average of the emission profiles inside the observation bandwidth and an equal bandwidth of continuum. The resulting profile was multiplied by the effective primary beam and the visibility then calculated. The visibility curve of the continuum emission was calculated as well, and the visibility ratio (on the line compared to the continuum) as a function of baseline was then determined.

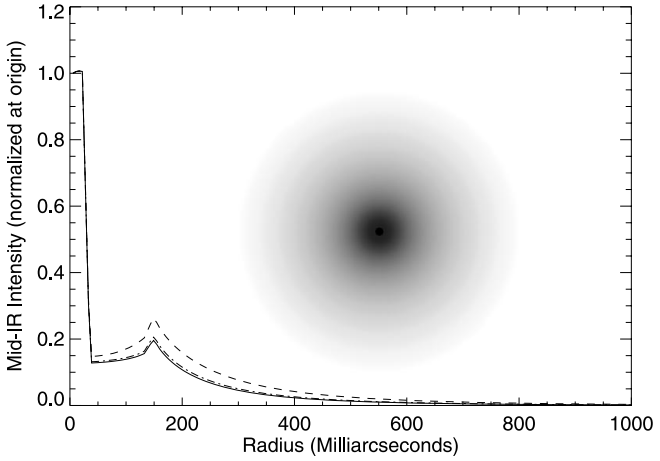

FIG. 2.—Example of the mid-IR emission as a function of radius from the star for one particular gas model, normalized to unity at radius 0. Solid line shows the radial profile for the dust continuum, while the dashed line represents the emission at the core of the absorption line. The dot-dashed line represents the emission after accounting for the finite-bandwidth and double-sideband detection. The inset image shows a two-dimensional representation of the absorption region defined by the ratio of the absorption core to the continuum profiles.

Figures 1–3 illustrate this entire process, showing example output at every stage of the analysis process for a silane line around IRC +10216. All subsequent model visibility ratios have been processed in an identical fashion, but these diagnostic plots are not presented, for brevity. The particular gas model shown in Figures 1–3 has a silane formation radius of only $10R_*$, small enough to produce a large change in the visibility on and off the spectral line. Since the filter-bank system measures a visibility ratio, the radial emission profiles were usually of only secondary interest, and more emphasis was placed on interpretations of ratios.

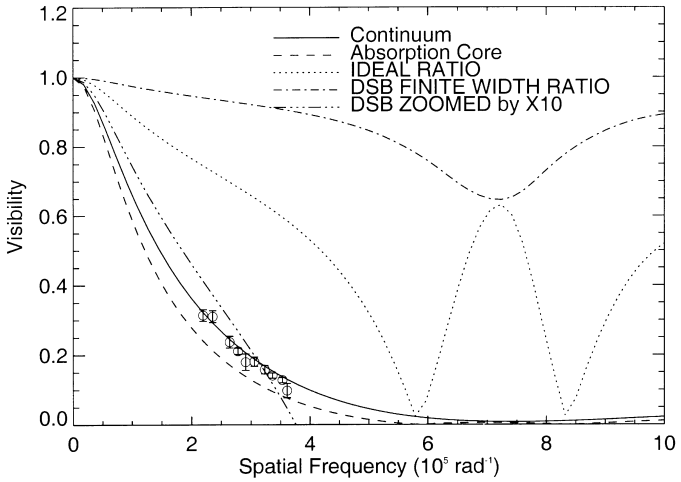

FIG. 3.—Visibility curves on and off a spectral feature. The dashed and solid lines represent the visibility curves on and off the absorption core, respectively; the dotted line shows the ratio. The dot-dashed line shows the visibility ratio after accounting for finite-bandwidth and double-sideband (DSB) detection. Deviations from unity are multiplied, or zoomed in, by a factor of 10, and shown by a triple-dot-dashed line; the zoom means that, for example, 0.6 now corresponds to 0.96 in the original units. The data points on this plot represent coeval visibility measurements of the dust continuum reported in Paper II.

To facilitate a better understanding of the visibility data, example brightness profiles appear in Figure 2. The bright spike at the origin is from stellar photospheric emission seen through the dust and gas, while the secondary peak at 150 mas reveals the location of the dust shell inner radius. It is important to note that while the star itself clearly shines through the dust envelope (it is the highest surface brightness feature of the nebula), it contributes a tiny percentage of the total mid-IR emission, because of the large emission from the dust shell. The inset image is a two-dimensional representation of the absorption region defined by the ratio of the absorption core to the continuum profiles. One can see that absorption for this model is indeed highest near the center of the dust shell. The basic point of the filter-bank experiment was to measure the size of this absorption region.

Figure 3 shows the visibility curves corresponding to the emission profiles of Figure 2. The various curves are described in the figure caption, and show the effects of applying the instrumental corrections discussed in this section. In this case, a visibility ratio of about 0.92 would be expected for the range of baselines observed (2–4 m).

The analysis process discussed above took into account all the practical details of the experiment: finite bandwidth, primary beam, double-sideband detection. The next sections present the data from the filter-bank experiment and detail the modeling results.

3. INTERFEROMETRY ON SPECTRAL LINES: RESULTS

Spectral line observations were carried out for two target sources, the carbon star IRC +10216 and the red supergiant VY CMa. General introductions to both of these stars, including discussions of previous continuum observations, can be found in Paper II. A summary of all the filter-bank data can be found in Figure 4; details will be discussed in subsequent sections. Recall from Paper I that the ratio of the visibility on the line compared to that off the line is made by dividing the fringe amplitude ratio by the

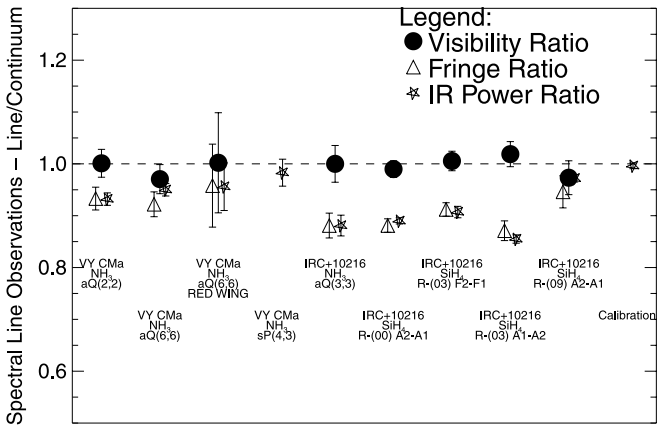

FIG. 4.—Summary of all the filter-bank data on spectral lines presented in this paper, from 22 full nights of observing in the fall of 1998. Each data point represents the average of multiple nights of observing at baselines between 2 and 4 m, with the molecular transition and target source indicated below each set of symbols. Observing details can be found in Tables 2 and 4. The triangles show the ratio of the fringe amplitude on and off the line, while the star symbols show the ratio of the total infrared (IR) signal on and off the line. The normalized visibility ratio on and off the spectral line results from dividing the fringe ratio into the IR power ratio, and appear in the figure as filled circles.

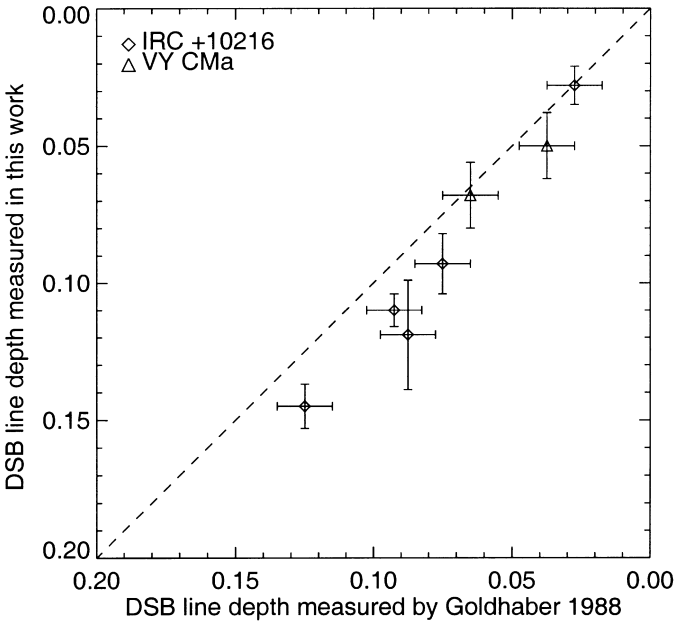

FIG. 5.—Comparison of the observed line depths of transitions observed by G88 and this work. The overall agreement is good, although there is clear evidence of a systematic difference. See § 3.1 for a discussion.

infrared power ratio. Hence, in Figure 4, the visibility ratios were derived from the fringe (amplitude) ratios and the IR power ratios, and do not represent an independent set of measurements. See tables of line frequencies in Monnier (1999, Tables C.4 and C.5) for more information regarding specific molecular transitions.

3.1. *Comparison with Previous Spectroscopic Results*

While the interferometric data presented here are the first of their kind, the depths of the spectral lines have been observed before. Figure 5 shows a comparison of all the lines observed with the double-sideband line depths observed by G88. While the agreement is good in general, there is a clear signal that the line depths measured in 1998 were slightly deeper around IRC +10216 than the mid-1980s observations of Goldhaber. There are many possible explanations for this. Changes in the dust shell geometry, molecular abundance, and different seeing conditions during the observations themselves can cause small changes in the line depth. However, the good overall agreement is confirmation that the circumstellar environments important for forming these spectral lines around both VY CMa and IRC +10216 have not changed radically in the last decade, justifying the use of previous modeling efforts (G88; KR93) in developing molecular gas models (see modeling step 2 in § 2.4).

4. IRC +10216

A journal of spectral line observations for IRC +10216 can be found in Table 2, while a full and concise summary of the data appears in Table 3. Separate modeling for both molecules, SiH_4 and NH_3, is presented below.

4.1. *Silane in IRC +10216*

4.1.1. *Previous Work*

The mid-IR transitions of silane around IRC +10216 have been observed by Goldhaber & Betz (1984), G88, KR93, and Holler (1999). Goldhaber and colleagues used a heterodyne spectrometer, which produced the highest spectral resolution data, fully resolving the absorption line cores (spectral resolution ~ 0.2 km s^{-1}). KR93 employed a Fourier transform spectrometer at Kitt Peak with somewhat lower spectral resolution, about 3 km s^{-1}, sufficient to determine the spectral line strengths but insufficient to fully resolve the cores. Holler used a broadband radio frequency (RF) spectrometer coupled to the heterodyne detection system of the ISI, resulting in sub–km s^{-1} spectral resolution (also see Isaak, Harris, & Zmuidzinas 1999). Because the line depths have remained largely unchanged over the last 15 yr, the modeling results of these workers was assumed to hold true today. The most detailed analysis can be found in KR93, and their gas model parameters were a starting point for the analysis that follows.

KR93 found a relative abundance of silane compared to molecular hydrogen of 2.2×10^{-7} with a rotational temperature law, $T_{\rm rot} = 2000r^{-0.525}$ (where r is expressed in units of stellar radii), which falls off slightly faster than the dust temperature. The calculated column density was 2.2×10^{15} cm^{-2}. In addition, $T_{\rm vib}$ was taken to be about 85% of the $T_{\rm rot}$, to match the weak emission observed in the higher J lines. These results assumed spherical symmetry, a uniform outflow of 14 km s^{-1} outside $20R_*$, and a microturbulent velocity of 1 km s^{-1}. It was found that the line ratios were much better fitted by truncating the silane distribution inside $40R_*$, and KR93 concluded that silane must be forming in the outflow at about this radius. With these assumptions, KR93 were able to satisfactorily match the line strengths of seven silane transitions and the spectral profile of one of Goldhaber's high spectral resolution profiles. Holler (1999) estimated the column density of SiH_4 from data taken in 1999 May using one ISI telescope and found it consistent with previous measurements ($\sim 2.7 \times 10^{15}$ cm^{-2}).

4.1.2. *Visibility Observations*

Table 3 reports the visibility ratios on and off various silane absorption features in fall 1998. A stellar recessional velocity of $V_{\rm LSR} = -26.0$ km s^{-1} has been used to convert $V_{\rm LSR}$ to expansion velocity, based on G88. In all cases, the

TABLE 2

JOURNAL OF IRC +10216 SPECTRAL LINE OBSERVATIONS

Target Molecule	Target Transition	LO Molecule	LO Transition	LO Wavelength (μm)	Dates (UT 1998)
SiH_4.....	R-(00) $A2$–$A1$	$^{13}C^{18}O_2$	P(20)	10.945	Nov 5, Nov 6, Nov 13
SiH_4.....	R-(03) $F2$–$F1$	$^{13}C^{16}O_2$	R(10)	10.318	Oct 18, Oct 19, Nov 21
SiH_4.....	R-(03) $A1$–$A2$	$^{13}C^{18}O_2$	P(10)	10.853	Nov 4, Nov 10, Nov 14
SiH_4.....	R-(09) $A2$–$A1$	$^{13}C^{16}O_2$	R(30)	10.694	Oct 27, Oct 28, Nov 27, Dec 3, Dec 11
NH_3.....	aQ(3,3)	$^{12}C^{16}O_2$	P(34)	10.741	Oct 20, Oct 21, Oct 22, Nov 20

TABLE 3

SUMMARY OF IRC +10216 SPECTRAL LINE DATA

TARGET MOLECULE	TARGET TRANSITION	BANDWIDTH OF FILTER BANK		FRINGE AMPLITUDE RATIO	IR POWER RATIO	VISIBILITY RATIO
		MHz	km s^{-1}			
SiH_4	R-(00) $A2$–$A1$	180	1.97	0.881 ± 0.013	0.890 ± 0.006	0.990 ± 0.016
SiH_4	R-(03) $F2$–$F1$	180	1.86	0.912 ± 0.013	0.907 ± 0.011	1.006 ± 0.019
SiH_4	R-(03) $A1$–$A2$	180	1.95	0.871 ± 0.019	0.855 ± 0.008	1.019 ± 0.024
SiH_4	R-(09) $A2$–$A1$	180	1.93	0.946 ± 0.031	0.972 ± 0.007	0.973 ± 0.033
NH_3	aQ(3,3)	180	1.93	0.881 ± 0.024	0.881 ± 0.020	1.000 ± 0.035

NOTE.— The filter-bank bandpass was centered at $V_{LSR} = -40$ km s^{-1} for all observations. Each ratio represents the value of the absorption feature with respect to nearby stellar continuum at baselines between 2 and 4 m.

visibility ratio has been observed to be consistent with unity, and data from all baselines (2–4 m) have been averaged together. Qualitatively, this implies that the absorption region is large compared to the spatial resolution of the interferometer baseline, $\sim 0''.4$.

The model for the molecular envelope developed in KR93 was combined with the new dust shell model from Paper II as a starting point for this modeling work. In particular, the same power-law relation for the rotational temperature was used, and the vibrational temperature was set equal to 85% of the dust temperature. A microturbulent velocity of 0.6 km s^{-1} was used to match the line widths observed by G88. Next, a series of gas models was calculated using different silane formation radii: $10R_*$, $40R_*$, and $80R_*$. The silane abundances were then scaled to match the average line depths of the observed transitions. For each of these three gas models and for all four observed lines, the visibility ratios of the line compared to the continuum were calculated and compared to observations.

The results of these models appear in Figure 6. Indeed, gas models with the largest formation radii fit the line depths of the four lines the best, as found by KR93, implying a relatively low overall rotational temperature of the absorbing molecules. In addition, the importance of the visibility ratio observations made with the ISI and filter bank can be seen. For formation radii less than about $40R_*$, the predicted visibility ratios are significantly below unity. Even for a formation radius of $40R_*$ (the choice preferred by KR93 based on spectroscopy alone), the visibilities in the spectral lines are too small to be consistent with observations (although not strongly ruled out). The column density for the most favored $80R_*$ model was found to be 1.3×10^{15} cm^{-2} (2.0×10^{15} cm^{-2} for the $40R_*$ case).

Since we have measurements of four lines of differing rotational excitation energies, the sensitivity of the visibility ratios to the rotational temperature law can be investigated. Models with identical gas density distributions were run using $T_{rot} = T_{vib} = T_{dust}$, and the results for these calculations can be found in Figure 7. This temperature law does not fit the line depths as well as the first set of models, supporting the adoption of the empirical temperature falloff of KR93. Alternatively, the population of low-lying J transitions could be enhanced if the mass-loss rate was higher in the past; this would have the effect of increasing the density of cold silane, increasing the molecular absorption from the ground state. The visibility ratios are similar to those found in the KR93-based models above, and the earlier conclusion of a large molecular formation radius is supported and now shown to be insensitive to choice of temperature profile.

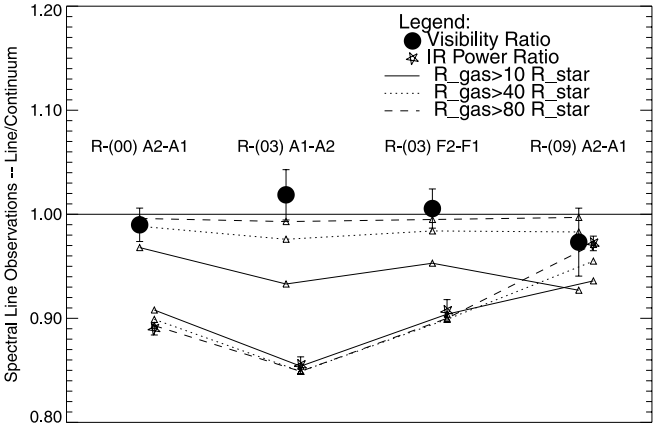

FIG. 6.—Results of modeling the IR power and visibility data for silane around IRC +10216 using the temperature laws derived in KR93. Filter-bank data appear as points with error bars, while model results are represented by small triangles connected by lines corresponding to different molecular density distributions, as marked. The transitions are presented, from left to right, in order of increasing excitation energy. The top points and lines correspond to the visibility ratios of the absorption line with respect to the continuum, while the bottom data points and lines correspond to the observed and modeled line depths. The solid line shows a model with silane forming at $10R_*$. The dotted and dashed lines show molecular formation radii of $40R_*$ and $80R_*$, respectively.

4.1.3. *Conclusions*

In short, the filter-bank observations largely confirm the conclusions of KR93; namely, that silane must be forming

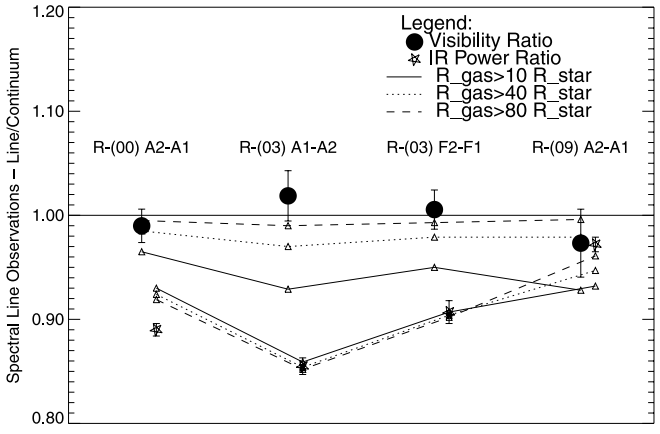

FIG. 7.—Same as Fig. 6, but assuming $T_{rot} = T_{dust}$

at a large distance from the star. The visibility data directly measure the size of the absorption region to be larger than $\sim 0\farcs4$ and favor a formation radius even larger than that proposed by KR93. The combination of spectroscopy and interferometry convincingly demonstrates that silane is forming at a radius of $\gtrsim 80R_*$. The visibility data are only able to set a lower limit on the formation radius, since no visibility difference on and off the line was detected within the experimental uncertainty.

For the stellar radius of 22 mas used in the model and a distance of 135 pc, $80R_*$ corresponds to about 240 AU from the star. It is not clear why silane would begin to form at so remote a location in the outflow. The densities of the atomic constituents of silane are proportional to r^{-2} for a uniformly expanding envelope and would act to shut off chemical reactions that are density dependent. If silane is formed on the surfaces of grains, then the gas-phase density of silicon (and its compounds) may not be as important as the amount of gas-phase silicon and H_2 adsorbed onto grains. Adsorption of H_2 on the grain surfaces would probably be small at the higher temperatures (1000–1400 K) where dust forms, and be more pronounced at larger distances from the star (see, e.g., the calculations of Leitch-Devlin & Williams 1985). In these models, the temperatures of the gas and dust are about ~ 290 K at $40R_*$ and 200 K at $80R_*$.

Gas-phase SiS, which forms in abundant quantities in the photosphere, has been predicted to be depleted significantly by adsorption onto grains (Glassgold & Mamon 1992). In fact, depletion of SiS within $100R_*$ has already been observed in both mid-IR (Boyle et al. 1994) and millimeter-wave transitions (Bieging & Nguyen-Quang-Rieu 1989; Bieging & Tafalla 1993). We hypothesize that the large radius of SiH_4 creation is related to the timescale for this depletion process and/or the adsorption of H_2 onto grains. It is hoped that the introduction of these new observations will stimulate renewed theoretical interest in understanding both the chemical origins and lineage behind the high abundance of silane around IRC +10216.

4.2. *Ammonia in IRC +10216*

4.2.1. *Previous Work*

The mid-IR rovibrational transitions of ammonia around IRC +10216 have been observed by B79, G88, KR93, and Holler (1999). Some details regarding the spectrometers employed have already been summarized in § 4.1.1. Because the line depths have remained essentially unchanged over the last 15 yr, the modeling results of these workers are again assumed to be valid today. As in the case for silane, the most detailed analysis can be found in KR93, and their gas model parameters acted as a starting point for the analysis that follows.

KR93 found a relative abundance of ammonia compared to molecular hydrogen of 1.7×10^{-7} with a rotational temperature profile $T_{\rm rot} = 2000r^{-0.60}$ (where r is expressed in units of stellar radii), a faster fall-off than the profile used for silane. Even with this steeper fall-off, the predicted depth of the lowest lying $aR(0, 0)$ line was much weaker than that observed, requiring either much colder or more dense gas in the outer envelope ($\gtrsim 400R_*$). The calculated column density was 2×10^{15} cm^{-2}, very similar to recent results from Holler (1999; $\sim 2.2 \times 10^{15}$ cm^{-2}). These results assumed spherical symmetry, a uniform outflow of 14 km s^{-1} outside $20R_*$, and a microturbulent velocity of 1 km s^{-1}. Since a fit of the larger width of the high-excitation $aQ(6, 6)$ line with a constant velocity flow was not possible, a more complicated velocity model was used, which had the gas accelerating to terminal velocity at radii between $5R_*$ and $20R_*$ (see Figs. 3*a* and 11 in KR93 for the velocity and density laws adopted).

Although unable to reproduce the line shapes in precise detail, the KR93 models were successful at qualitatively explaining the bulk of the spectroscopic observations available by placing the ammonia density peak around $12R_*$. Importantly, these models represent ideal test cases for the filter-bank experiment, because the presence of ammonia absorption inside of $20R_*$ is expected to be clearly indicated by its visibility.

4.2.2. *Results*

Table 3 shows the ratio of the visibilities observed in and out of the $aQ(3, 3)$ NH_3 absorption feature in the fall of 1998. A stellar recessional velocity of $V_{\rm LSR} = -26.0$ km s^{-1} has been used to convert $V_{\rm LSR}$ to expansion velocity, based on G88. The filter-bank bandpass selected (~ 1.9 km s^{-1}) was somewhat smaller than the full-width half-depth (FWHD) observed by G88, about 5 km s^{-1}, and centered on the absorption core, corresponding to an outflow velocity of 14 km s^{-1}. In this case, as for the silane observations, the visibility ratio was observed to be consistent with unity.

The modeling process began with the dust shell model from Paper II and the gas model developed in KR93. The same power-law relation for the rotational temperature and a 1.0 km s^{-1} microturbulent velocity were initially used. An ammonia density and velocity distribution similar to KR93 were used, although simplified. Specifically, the velocity was increased linearly from 0.1 to 14 km s^{-1} between 3 and 20 R_*. The ammonia density profile used started at $5R_*$, peaked at $\sim 10R_*$, and decreased outside $20R_*$, consistent with a uniform outflow ($\rho \propto r^{-2}$). This corresponded to a linearly increasing ammonia shell mass until $20R_*$, where uniform outflow was assumed to begin. See Figure 8 for a plot of the density profile used.

As was shown for silane in the last section, significant molecular absorption inside about $20R_*$ necessarily results

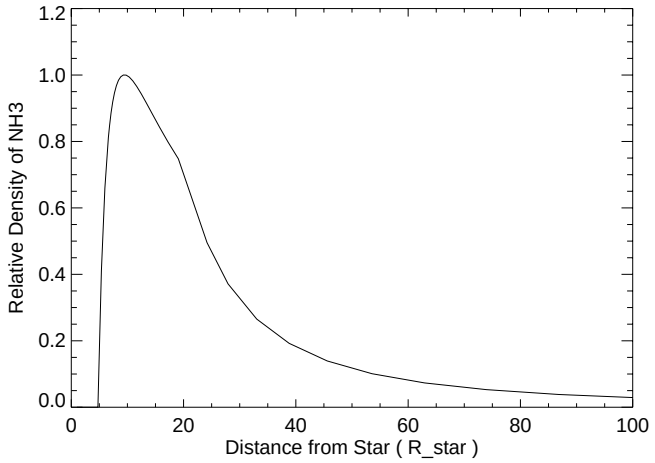

FIG. 8.—Relative density of ammonia as a function of radius for the IRC +10216 gas model (based on KR93). The outflow velocity was increased linearly between 0.1 and 14 km s^{-1} between $3R_*$ and $20R_*$. Using this velocity law and the density of ammonia shown by the solid line, the ammonia shell mass increases linearly with radius from $5R_*$ until $20R_*$, at which point it becomes constant, consistent with uniform outflow. The visibility data reported in this paper rule out this model.

in substantial differences in interferometric visibilities on and off the spectral line. Figure 9 shows the spectral profile and visibility ratio for the above model of ammonia around IRC +10216, based on KR93, and also the spectral line data taken from G88. KR93 did not model this specific transition, so the agreement cannot be expected to be precise; indeed, the line prediction is narrower than the profiles observed by Goldhaber. The density of ammonia has been adjusted to match the line depth observed in fall 1998 within the bandpass of the ISI filter bank, resulting in a column density of 8.4×10^{15} cm^{-2} for this model.

The model visibility ratio at a spatial frequency of 3×10^5 rad^{-1} is 0.926, compared to the observed ratio of 1.000 ± 0.035. This model is thus ruled out at a 2 σ level. This reinforces a conclusion from the modeling of silane: significant molecular absorption occurring within about $20R_*$ for IRC +10216 results in a strong on-line and off-line difference in the interferometric visibilities, a signal not seen with the ISI filter-bank experiment. The conclusion that ammonia forms at a distance of $\gtrsim 20R_*$ from the star indicates that, as in the case of silane, ammonia molecules do not form near where the dust condenses, but rather at lower temperatures and probably through surface adsorption. The dust grain temperature at $20R_*$ is $\sim$400 K in these models.

4.2.3. *Discussion*

There are other, purely spectroscopic, observations that also suggest that the explanation put forth by KR93 for the broad *aQ*(6, 6) line, bulk acceleration of gas within $20R_*$, may not be fully correct. KR93 did not attempt to fit the high spectral resolution profiles published in G88, which revealed details concerning the ammonia around IRC +10216 not reproduced by models relying on accelerating gas to broaden the absorption lines.

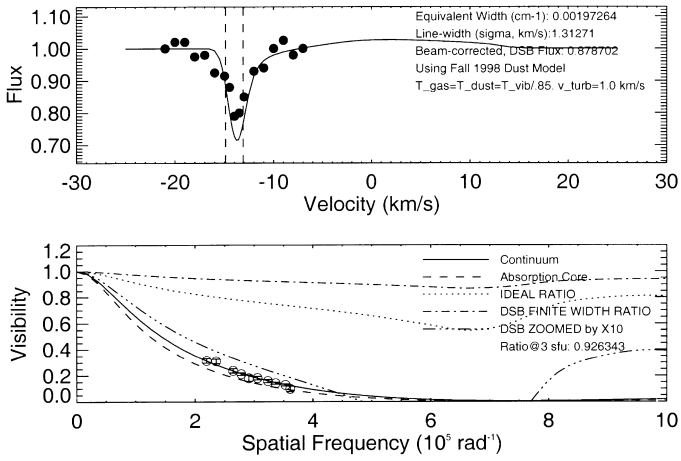

FIG. 9.—Results of modeling the IR power and visibility data for ammonia *aQ*(3, 3) transition around IRC +10216, based on parameters derived in KR93. *Top*: Model spectral line profile convolved with the instrument response along with the observations of G88. *Bottom*: Model visibility curves on and off the spectral feature; can be compared to the observed dust continuum data (*open circles*; see Paper II). The dashed and solid lines show the visibility curves on and off the absorption core (defined by the vertical dashed lines in the top panel) respectively; the dotted line shows the ratio. The dot-dashed line shows the visibility ratio after accounting for finite-bandwidth and double-sideband (DSB) detection. Deviations from unity are multiplied, or zoomed in, by a factor of 10, and shown by a triple-dot-dashed line; the zoom means that, for example, 0.6 now corresponds to 0.96 in the original units.

KR93 fitted the *aQ*(6, 6) line data originally published in B79, which was cut off at -17 km s^{-1} relative to the stellar velocity. Features broadened due to absorption by gas in the acceleration region would be asymmetric, with a sharp blue edge and significant redshifted absorption by hot gas. Indeed, the model profiles of KR93 show this telltale characteristic (see Fig. 13 of KR93), but were unconstrained by the incomplete B79 published profile. Complete line profiles, including the full blue wing of the absorption feature, were published in G88, revealing a rather symmetric line—at odds with KR93 model results.

Thus far, the line-width data from G88 cannot be reproduced in detail with this class of models, independent of the visibility data. The line widths were observed to increase with the energy of the rotational level. The 1 σ widths were measured to be 0.8, 1.7, and 3.1 km s^{-1} for the *aR*(0, 0), *aQ*(2, 2), and *aQ*(6, 6) transitions, respectively, while the relative velocity of the core remained constant to within $\sim$1 km s^{-1}. While a near-star acceleration law and suitably peaked ammonia distribution can be adjusted to reasonably fit the line width of any single transition (e.g., Fig. 9), the large increase between the *aQ*(2, 2) and *aQ*(6, 6) lines is not reproduced. Furthermore, lines broadened by accelerating gas should show significant shifts in the location of the core as a function of excitation energy.

The presence of decaying gas turbulence outside the acceleration region may qualitatively explain the line-width behavior and the lack of a significant difference in the visibilities. The inner dust shell of IRC +10216 is already known to be quite clumpy in near-IR images (Weigelt et al. 1998; Haniff & Buscher 1998; Tuthill, Monnier, & Danchi 1998; Monnier 1999; Tuthill et al. 2000). Furthermore, dynamical models of dust shell production in carbon stars lead to large velocity dispersion as the individual shells of dust are accelerated (Winters et al. 1995, 1998; Weigelt et al. 1998). Both turbulence and velocity gradients across individual dust shells (clumps) will cause significant broadening of lines formed in these regions. Under these conditions, one would also expect the Doppler velocity of the core to be nearly constant, consistent with observations, but the line widths would naturally decrease for lines forming further in the outflow as sound waves (or weak shocks) bring the outflow into hydrostatic equilibrium. The dynamical dust shell models of Winters et al. could be coupled with the radiative transfer code of Keady to quantitatively test these suppositions (as for CO in Winters et al. 1998).

There are other potential explanations for why absorption lines by high-*J* states are much broader than for lower excitation states. For instance, if the high-*J* states are populated by shock heating, one would expect a higher velocity dispersion due the turbulence and velocity shifts accompanying shocks. This class of explanation, whereby the excitation mechanism (and possibly even the *formation* mechanism) is directly related to peculiar *local* conditions (e.g., shocks, high velocity dispersion), needs further consideration.

4.3. *Summary for IRC +10216*

The narrow line widths of all the silane lines and the lack of an interferometric signal place the location of silane formation at or beyond $\sim 80R_*$ outside the turbulent inner envelope. In addition, the lack of interferometric signal and the broad (symmetric) lines of ammonia place their formation outside $\sim 20R_*$, beyond the gas acceleration region,

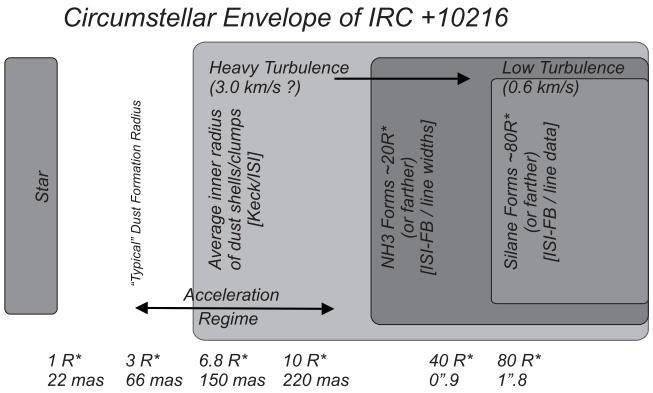

FIG. 10.—Likely sites of silane and ammonia formation around IRC +10216, based on the results of this paper and previous spectral line work. Importantly, the data suggest that the outflow remains quite turbulent and/or clumpy significantly beyond the acceleration region. The observations undergirding each major element of this schematic are listed in brackets (Keck: near-IR speckle work [Tuthill et al. 2000]; ISI: ISI continuum data [Paper II]; ISI-FB: ISI filter-bank data [this work]).

but in a turbulent (or clumpy) flow. These ideas are illustrated schematically in Figure 10 and represent a significant improvement in our knowledge of the molecular stratification around IRC +10216.

5. VY CMa

While no silane has been observed in the oxygen-rich stellar wind of the red supergiant VY CMa, many absorption lines of ammonia have been. A journal of these spectral line observations made with the ISI filter bank can be found in Table 4.

5.1. *Previous Work*

The mid-IR transitions of ammonia around VY CMa were first observed by McLaren & Betz (1980). However, a larger set of data with better frequency coverage was published by G88, and these data have been used for subsequent consideration. Details regarding the capabilities of the heterodyne spectrometer employed can be found in § 4.1.1. While McLaren & Betz reported a significant change in the line profile of NH_3 $aQ(2, 2)$ between 1978 October and 1979 December, the profile reported by G88 observed in 1982 September is nearly identical to the 1979 December data. In addition, the G88 line depth is consistent with the spectral data obtained by the filter bank in this paper (see Table 5). In light of this consistency, we have assumed that the G88 line profiles are still representative of the current epoch.

All of the lines, $aR(0, 0)$, $aQ(2, 2)$, $aQ(3, 3)$, and $aQ(6, 6)$, observed by G88 possessed broad absorption features with 1 σ widths of $\sim$3.8 km s^{-1}. The cores of the lines were centered around $V_{LSR} \sim -6$ km s^{-1}, with the high excitation line cores being slightly less blueshifted. Assuming a stellar recessional velocity of $V_{LSR} = 22.3$ km s^{-1} (based on maser data), this corresponds to an outflow rate of $\sim$29 km s^{-1}. Using these lines, G88 estimated a column density of ammonia of $(6 \pm 4) \times 10^{15}$ cm^{-2} using a simple model based on the Sobolev approximation. We have repeated these calculations using a similar gas model with the Keady code.

5.2. *Results and Models*

Table 5 shows the visibility ratios observed on and off a number of NH_3 absorption features in the fall of 1998. A stellar recessional velocity of $V_{LSR} = 22.3$ km s^{-1} has been used to convert V_{LSR} to expansion velocity, based on G88. The filter-bank bandpasses selected were set to equal the FWHD observed by G88, and were centered on the absorption cores. Data in Table 5 represent a nondetection of the $sP(4, 3)$ line, which also had not been detected by any previous measurements. Just as for IRC +10216 (see Table 3), the visibility ratios were observed to be consistent with unity. In addition to the full $aQ(6, 6)$ absorption line, the red half of the line was observed separately in the hopes of observing the location of any accelerating gas. However, the signal-to-noise ratio for this measurement ($\sim$10) was not high enough to justify further modeling.

A simple gas model based on the line fit of the $aR(0, 0)$ line in G88 was developed using the new VY CMa dust shell model of Paper II. Unlike the case for IRC +10216, the line widths for the NH_3 lines around VY CMa were all roughly the same. This fact, and the fact that the line core locations only showed a slight shift with excitation energy, support a model in which the absorption lines all form mostly outside the acceleration region. Therefore, a constant-outflow model was adopted, using an expansion velocity of 29 km s^{-1}, which matched the profiles of the $aQ(2, 2)$ and $aQ(6, 6)$ lines; the broad line widths were created by model microturbulence of 3.5 km s^{-1}.

The temperature of the $J = K$ rotational states is controlled either by collisions, due to the lack of dipole transitions from these states to lower J, or by IR pumping in the 6.1 μm band (see § 2.3.2). During modeling, this temperature profile is normally varied using a power law (as by KR93) to empirically fit the line depth ratios. Unfortunately, there were an insufficient number of lines available in this case to utilize this strategy. An alternative scheme, in which two temperature profiles were assumed to represent reasonable limits, was used here:

1. The rotational temperature was set equal to the dust temperature, $T_{rot} = T_{dust}$. This corresponds to full coupling of the internal degrees of freedom of the gas molecules to the radiation field.

TABLE 4

JOURNAL OF VY CMa SPECTRAL LINE OBSERVATIONS

Target Molecule	Target Transition	LO Molecule	LO Transition	LO Wavelength (μm)	Dates (UT 1998)
NH_3	$aQ(2, 2)$	$^{13}C^{16}O_2$	$R(24)$	10.738	Oct 20, Oct 21, Oct 22, Nov 25
NH_3	$sP(4, 3)$	$^{13}C^{16}O_2$	$P(30)$	11.262	Oct 27
NH_3	$aQ(6, 6)$	$^{13}C^{16}O_2$	$R(18)$	10.784	Oct 18, Oct 19, Oct 28, Nov 5, Nov 24, Dec 11

TABLE 5

SUMMARY OF VY CMa SPECTRAL LINE DATA

TARGET MOLECULE	TARGET TRANSITION	BANDWIDTH OF FILTER BANK		FRINGE AMPLITUDE RATIO	IR POWER RATIO	VISIBILITY RATIO
		MHz	km s^{-1}			
NH_3	$aQ(2,2)$	540	5.80	0.933 ± 0.022	0.932 ± 0.012	1.001 ± 0.027
NH_3	$sP(4,3)$	420	4.73	N/A	0.983 ± 0.026	N/A
NH_3	$aQ(6,6)$	540	5.82	0.922 ± 0.024	0.950 ± 0.012	0.971 ± 0.028
NH_3	$aQ(6, 6)$[a]	180	1.94	0.958 ± 0.080	0.956 ± 0.046	1.002 ± 0.097

NOTE.—The filter-bank bandpass was centered at $V_{LSR} = -7$ km s^{-1} for all observations, except when observing the red half of $aQ(6, 6)$ ($V_{LSR} = -6$ km s^{-1}). Each ratio represents the value of the absorption feature with respect to the nearby stellar continuum at baselines between 2 and 4 m.

[a] Red half.

2. $T_{rot} = T_* r^{-0.60}$, where r is expressed in units of stellar radii. This choice is similar to that found empirically for ammonia around IRC +10216 by KR93. While VY CMa and IRC +10216 do have similar mass-loss rates (within a factor of $\sim$10), the differing chemistry (O-rich versus C-rich) may affect the cooling rates, and this ad hoc temperature profile is clearly rather speculative.

Because G88 in most cases did not publish the emission components of the NH_3 transitions, we were not able to model this aspect of the line profile. Instead we followed KR93 (for IRC +10216) and suppressed emission in our model profiles by assuming that the vibrational temperature was 85% of the dust temperature.

Figure 11 shows the results assuming $T_{rot} = T_{dust}$. The high optical depth at 11 μm ($\tau \sim 2.4$; see Paper II) effectively shields the inner dust and molecular envelope from view. The $\tau_{dust} = 1$ surface is located at about $12R_*$ along the central impact parameter, and hence most of the observed continuum emission is occurring outside of this. This explains why none of the models with molecular formation radii between 10 and 80 R_* were decisively ruled out with the interferometry data of Figure 11. However, one can see that for this assumed temperature law, the line ratios were best fitted by a molecular formation radius outside $\sim 40R_*$. Interestingly, this distance corresponds to the extent of the acceleration region deduced from proper-motion studies of the H_2O masers (Marvel 1996; Richards, Yates, & Cohen 1998). Figure 12 shows the results for the temperature profile of case 2, assuming $T_{rot} = T_* r^{-0.60}$; the same general conclusions still apply, showing that they are not highly model dependent. It is worth noting that the equivalent widths for models with small molecular formation radii (especially for $10R_*$) were systematically higher than those measured by G88. While the line depths in the filter-bank bandpass were fitted by increasing the ammonia density, the line widths themselves were not. Ideally, the microturbulence parameter should be adjusted for each set of molecular formation radii to compensate for differing line-broadening effects, such as thermal broadening and the finite size of the continuum source. Such adjustments did indeed improve the quality of these fits, but significantly increased the complexity of the modeling, while only weakly affecting the line and visibility ratios.

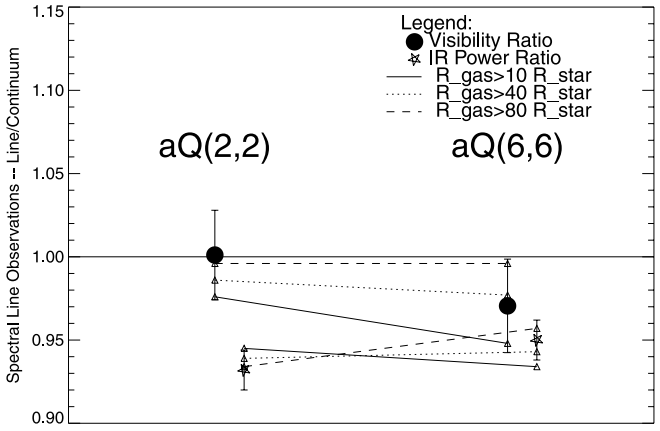

FIG. 11.—Results of modeling the IR power and visibility data for ammonia around VY CMa, assuming $T_{rot} = T_{dust}$. Filter-bank data appear as points with error bars, while model results are represented by small triangles connected by lines corresponding to different molecular density distributions, as marked. The top points and lines correspond to the visibility ratios of the absorption line with respect to the continuum, while the bottom data points and lines correspond to the observed and modeled line depths. The solid line shows a model with silane forming at $10R_*$. The dotted and dashed lines show molecular formation radii of $40R_*$ and $80R_*$, respectively.

5.3. *Discussion*

We conclude that NH_3 probably forms near the termination of the acceleration phase in the circumstellar envelope

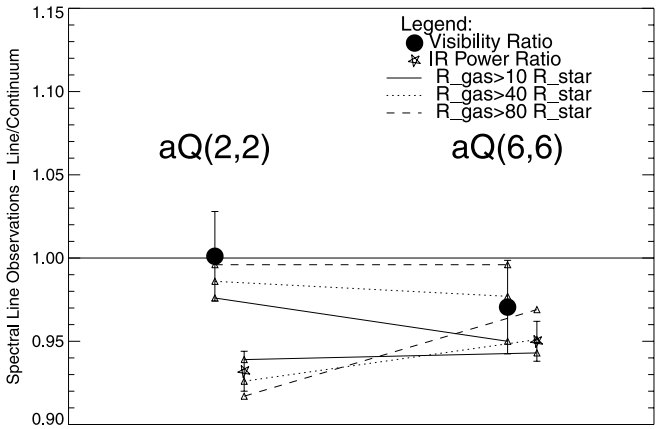

FIG. 12.—Similar to Fig. 11, but assuming $T_{rot} = T_* r^{-0.60}$, where r is in units of stellar radii.

of VY CMa ($\sim 40R_*$). This hypothesis is supported by the following observations:

1. Weak (but nonnegligible) correlation of absorption core velocity with excitation energy suggests that ammonia exists to a limited degree in the acceleration region.
2. Line ratios of the $aQ(2, 2)$ and $aQ(6, 6)$ transitions were best fitted by molecular formation radii $\gtrsim 40R_*$, a result found to be insensitive to the rotational temperature profile.
3. The visibility data for the high-excitation $aQ(6, 6)$ line marginally supports a large molecular formation radius, but the high optical depth of the dust shell makes the interferometric data relatively insensitive to absorption in the inner circumstellar envelope.

Around IRC +10216, high-excitation NH_3 lines were observed to be significantly broader than for the low-lying J states. Interestingly, this behavior was *not* duplicated for NH_3 around VY CMa. Unlike the case for IRC +10216, it appears that ammonia is forming at least partly in the acceleration region around this star, and hence the line formation of all the transitions is more affected by large turbulence in this region. Alternatively, the highly asymmetric inner dust shell seen in the near-IR (Monnier et al. 1999) and hinted at by ISI visibility data (Paper II) may be influencing the line formation characteristics. If the outflow is significantly asymmetric, line widths will be clearly affected by the varying projected outflow velocities of absorbing gas. Continued monitoring of water masers in the inner dust shell may clarify the gas dynamics and level of gas turbulence. This information will be critical for further progress in understanding the geometry of the molecular envelope around VY CMa.

6. CONCLUSIONS

We have presented the first interferometric results on mid-IR spectral lines around evolved stars. Specific results for the carbon star IRC +10216 and the red supergiant VY CMa have been summarized in previous sections. In addition, a few general conclusions can be drawn:

1. The formation radii of silane and ammonia are significantly beyond the dust formation zone for both evolved stars examined here.
2. Since dust formation by itself does not catalyze formation of these molecules, some other physical mechanism(s), still unknown, must be at play. Probably the adsorption of gas-phase molecules (e.g., SiS or H_2) onto grains sets the time/length scale for the important chemical reactions occurring on the grain surfaces.
3. When coupled with spectroscopic observations, these results indicate that turbulence, or velocity dispersion, is quite high in the inner envelope and is more likely to be responsible for the broad line widths of high excitation transitions than bulk acceleration.

The authors would like to recognize W. Fitelson, C. Lionberger, and M. Bester for important contributions to the construction and software development of the filter bank, and K. McElroy for observing assistance. We also acknowledge productive discussions with A. Glassgold and A. Betz. J. D. M. also would like to thank J. Keady for kindly allowing his sophisticated radiative transfer code to be used for this project, and for many stimulating discussions about the molecules of IRC +10216. This work is part of a long-standing interferometry program at U.C. Berkeley, supported by the National Science Foundation (grants AST 92-21105, AST 93-21289, and AST 97-31625) and by the Office of Naval Research (OCNR N00014-89-J-1583).

REFERENCES

Betz, A. L., McLaren, R. A., & Spears, D. L. 1979, ApJ, 229, L97 (B79)
Bieging, J. H., & Nguyen-Quang-Rieu. 1989, ApJ, 343, L25
Bieging, J. H., & Tafalla, M. 1993, AJ, 105, 576
Boyle, R. J., Keady, J. J., Jennings, D. E., Hirsch, K. L., & Wiedemann, G. R. 1994, ApJ, 420, 863
Burrows, A., & Sharp, C. M. 1999, ApJ, 512, 843
Cherchneff, I., & Glassgold, A. E. 1993, ApJ, 419, L41
Danchi, W. C., Bester, M., Degiacomi, C. G., Greenhill, L. J., & Townes, C. H. 1994, AJ, 107, 1469
Glassgold, A. E. 1998, in IAU Symp. 191, Asymptotic Giant Branch Stars, ed. T. Le Berte, L. Libre, & C. Waelkens (San Francisco: ASP), 337
Glassgold, A. E., & Mamon, G. A. 1992, in Chemistry and Spectroscopy of Interstellar Molecules, ed. D. K. Bohme (Tokyo: Univ. Tokyo Press), 261
Goldhaber, D. M. 1988, Ph.D. thesis, Univ. California at Berkeley (G88)
Goldhaber, D. M., & Betz, A. L. 1984, ApJ, 279, L55
Gray, D. L., Robiette, A. G., & Johns, J. W. 1977, Mol. Phys., 34, 1437
Haniff, C. A., & Buscher, D. F. 1998, A&A, 334, L5
Holler, C. 1999, Master's thesis, Ludwig-Maximilians-Univ.
Isaak, K., Harris, A. I., & Zmuidzinas, J. 1999, in ASP Conf. Ser. 156, Highly Redshifted Radio Lines, ed. C. L. Carilli et al. (San Francisco: ASP), 86
Keady, J. J. 1982, Ph.D. thesis, New Mexico State Univ.
Keady, J. J., Hall, D. N. B., & Ridgway, S. T. 1988, ApJ, 326, 832
Keady, J. J., & Ridgway, S. T. 1993, ApJ, 406, 199 (KR93)
Lafon, J.-P. J., & Berruyer, N. 1991, A&A Rev., 2, 249
Lafont, S., Lucas, R., & Omont, A. 1982, A&A, 106, 201
Leitch-Devlin, M. A., & Williams, D. A. 1985, MNRAS, 213, 295
Marvel, K. B. 1996, Ph.D. thesis, New Mexico State Univ.
Mathis, J. S., Rumpl, W., & Nordsieck, K. H. 1977, ApJ, 217, 425
McLaren, R. A., & Betz, A. L. 1980, ApJ, 240, L159
Mihalas, D., Kunasz, P. B., & Hummer, D. G. 1975, ApJ, 202, 465
Monnier, J. D. 1999, Ph.D. thesis, Univ. California at Berkeley
Monnier, J. D., Danchi, W. C., Hale, D. S., Lipman, E. A., Tuthill, P. G., & Townes, C. H. 2000a, ApJ, 543, 861
Monnier, J. D., Fitelson, W., Danchi, W. C., & Townes, C. H. 2000b, ApJS, 129, 421 (Paper I)
Monnier, J. D., Tuthill, P. G., Lopez, B., Cruzalebes, P., Danchi, W. C., & Haniff, C. A. 1999a, ApJ, 512, 351
Nakanaga, T., Kondo, S., & Saeki, S. 1985, J. Mol. Spectrosc., 112, 39
Richards, A. M. S., Yates, J. A., & Cohen, R. J. 1998, MNRAS, 299, 319
Shu, F. H. 1991, The Physics of Astrophysics, Vol. 1: Radiation (Mill Valley: University Science Books)
Townes, C. H., & Schawlow, A. L. 1975, Microware Spectroscopy (New York: Dover)
Tuthill, P. G., Monnier, J. D., & Danchi, W. C. 1998, in IAU Symp. 191, Asymptotic Giant Branch Stars, ed. T. Le Berte, L. Libre, & C. Waelkens (San Francisco: ASP), 331
Tuthill, P. G., Monnier, J. D., Danchi, W. C., & Lopez, B. 2000, ApJ, in press
Urban, S., Papousek, D., Kauppinen, J., Yamada, K., & Winnewisser, G. 1983, J. Mol. Spectrosc., 101, 1
Weigelt, G., Balega, Y., Bloecker, T., Fleischer, A. J., Osterbart, R., & Winters, J. M. 1998, A&A, 333, L51
Willacy, K., & Cherchneff, I. 1998, A&A, 330, 676
Winters, J. M., Fleischer, A. J., Gauger, A., & Sedlmayr, E. 1995, A&A, 302, 483
Winters, J. M., Keady, J. J., Fleischer, A. J., & Gauger, A. 1998, in ASP Conf. Ser. 135, A Half Century of Stellar Pulsation Interpretation, ed. P. A. Bradley & J. A. Guzik (San Francisco: ASP), 337
Wolfire, M. G., & Cassinelli, J. P. 1986, ApJ, 310, 207